Convection in Io's Asthenosphere: Redistribution of Non-uniform Tidal Heating by Mean Flows

Paul J. Tackley

Department of Earth and Space Sciences, University of California, Los Angeles

Abstract. Numerical simulations of convection in a wide domain with spatially-varying internal heating intended to mimic tidal dissipation in Io's proposed asthenosphere are performed in order to better understand the convective dynamics, and in particular to quantify the relationship between surface observables (particularly the distribution of heat flux) and tidal dissipation. Two-dimensional calculations at high internal heating Rayleigh number Ra_Q of up to 10^{10} indicate a mean, domain-wide flow with superimposed small-scale instabilities. The mean flow spreads out the tidally-dissipated heat, resulting in long-wavelength surface heat flux variations that decrease in proportion to $Ra_Q^{-0.21}$. This scaling is shown to apply to different domain widths and also to three-dimensional geometry. Power-law scalings are also obtained for velocities and temperatures. These mean flow scalings are also derived analytically. Scaling to Io's asthenosphere, long-wavelength heat flux variations of order several percent are predicted, with temperature variations of order 10s K and mean flow velocities of 50-5600 meters/year.

Introduction

Jupiter's moon Io is the most volcanically-active body in the solar system [*Lopes-Gautier et al.*, 1999] and is expected to be undergoing vigorous convection in its silicate mantle. This vigorous activity is thought to be driven by tidal dissipation associated with its slightly eccentric orbit around Jupiter forced by a tidal resonance with the moon Europa [*Cassen et al.*, 1982; *Peale et al.*, 1979; *Ross and Schubert*, 1986; *Ross and Schubert*, 1985; *Schubert et al.*, 1986; *Schubert et al.*, 1981; *Segatz et al.*, 1988; *Yoder*, 1979; *Yoder and Peale*, 1981].

The distribution of tidal dissipation within Io is certainly non-uniform but its details depend strongly on internal structure. The best-developed models of Io's internal structure and associated tidal dissipation were developed by [*Ross and Schubert*, 1985; *Ross et al.*, 1990; *Segatz et al.*, 1988]. They proposed two end-member models: dissipation in a homogeneous mantle, which would require a viscosity of ~10^{17} Pa.s and would be maximum at the poles and minimum at the equator, or dissipation in a 50-100 km thick asthenosphere, which would require a viscosity in the range 10^8-10^{12} Pa.s and would be maximum at the equator particularly in two lobes facing towards and away from Jupiter, and minimum at the poles. While other possibilities have been proposed (particularly [*Keszthelyi et al.*, 1999]), the associated tidal dissipation has not been calculated.

The key to determining which of these models is more realistic is the development of links between interior dissipation and surface features such as topography, mountains and volcanoes. [*Ross et al.*, 1990] tried to match the Voyager-derived topography assuming that heat delivery to the surface occurs vertically above heat input by dissipation, and obtained a preferred model of 2/3 asthenosphere and 1/3 mantle heating. However, the assumption of vertical heat delivery is questionable because convection is expected to spread out the heat somewhat (a process that is the major focus of this paper.) Observational constraints have been greatly enhanced by the Galileo mission [*Carr et al.*, 1998; *Lopes-Gautier et al.*, 1999; *McEwen et al.*, 1998a; *McEwen et al.*, 1998b]. These observations indicate that while the distribution of volcanoes and mountains does not display a strong distribution on first analysis [*Lopes-Gautier et al.*, 1999], distribution functions obtained by spatial averaging display strong patterns, with the volcano distribution resembling the asthenospheric heating function, and a mountain distribution that is similar but phase shifted by 90° in longitude [*Schenk and Hargitai*, 1998; *Schenk et al.*, 2000; *Tackley et al.*, 2001].

The first numerical simulations of mantle convection in Io were performed in three-dimensional (3-D) spherical geometry by [*Tackley et al.*, 2001] at internal heating Rayleigh number Ra_Q of up to $O(10^7)$. These confirmed the expectation that increased vigor of convection results in increased spreading out of the tidally-dissipated heat. However, the convective vigor in those calculations was many orders of magnitude below that thought to be appropriate for Io. The goal of this paper is to use 2-D calculations to reach a higher Rayleigh number regime (although still not as high as Io) and to develop scalings that allow extrapolation to Io's convective regime. The present paper focuses purely on convection in a 50-100 km thick asthenosphere, neglecting the rest of the mantle, except that the results could be scaled to whole mantle convection. The results and scalings obtained here are also applicable to any situation in which infinite-Prandtl number convection is driven by horizontally-varying heat sources.

Model and Method

A Cartesian domain with reflecting side boundaries is assumed. The upper and lower boundaries correspond to the base of a crust/lithosphere, and the top of a relatively high-viscosity, chemically-denser mantle, respectively, and are thus assumed to be rigid, and isothermal (top) or zero flux (bottom). Due to variations in surface temperature and likely variations in crust/lithosphere thickness the upper (isothermal) boundary condition is only an approximation, but is thought to be reasonable because in rigid lid convection the top of the convecting region is defined by a particular viscosity hence isotherm [*Moresi and Solomatov*, 1995; *Solomatov*, 1995]; furthemore the effects of the huge horizontal variation in internal heating rate is likely to swamp any effects due to horizontal variation in thermal boundary condition An aspect ratio of 15 is chosen for most of the cases, which for an asthenosphere depth of 100 km approximately corresponds to 1/8 the distance around Io,

which is the smallest distance between minima and maxima of the asthenosphere tidal dissipation function [*Segatz et al.*, 1988]. The actual effective aspect ratio could be much higher than this if the asthenosphere is thinner, so larger aspect ratios are also considered.

TABLE 1: Physical Properties for Io's asthenosphere

Parameter	Symbol	Value	Units
Density	ρ	3270	kg/m^3
Surface heat flux	F	2.4	W/m^2
Mean tidal dissipation*	<Q>	7.34×10^{-9}	W/kg
Asthenosphere thickness	D	50-100	km
Gravitational acceleration	g	1.8	m/s^2
Heat capacity	C_P	1200	$J\ kg^{-1}\ K^{-1}$
Thermal diffusivity	κ	1.0×10^{-6}	m^2/s
Thermal expansivity	α	3×10^{-5}	K^{-1}
Asthenosphere viscosity‡	η_{asth}	10^8 - 10^{12}	Pa s

*assuming a 100 km thick asthenosphere. For 50 km thick, <Q> is twice this.

‡For a 50 km thick asthenosphere. If 100 km thick, the range is 10^9-10^{12} Pa s.

Table 1 lists likely physical parameters for Io's asthenosphere, based on the model of [*Segatz et al.*, 1988]. Constant viscosity is assumed in this study, both to allow higher Rayleigh number to be reached with available computational resources, and because according to stagnant lid convection theory, convection is confined to a layer with viscosity variations less than one order of magnitude [*Moresi and Solomatov*, 1995] (the small temperature variations obtained in this study are compatible with this.) The melt-solid system is treated as a single one-phase system, consistent with findings from magma ocean modeling that crystal settling velocity (for separated crystals) is much smaller than convective velocities [*Solomatov and Stevenson*, 1993b]. Because the Prandtl number of rocks is effectively infinite even for a viscosity as low as 10^8 Pa.s, the usual equations for Boussinesq, infinite-Prandtl number, internally-heated convection, using the standard thermal non-dimensionalization (e.g., [*Parmentier et al.*, 1994; *Travis et al.*, 1990]), are used:

$$\vec{\nabla} \cdot \vec{v} = 0 \tag{1}$$

$$\nabla^2 \vec{v} - \vec{\nabla} p = Ra_Q T \hat{z} \tag{2}$$

$$\frac{\partial T}{\partial t} = \nabla^2 T - \vec{v} \cdot \vec{\nabla} T + Q(x,y,z) \tag{3}$$

Where $\vec{v}$ is velocity, p is pressure, T is temperature, t is time, $\hat{z}$ is a unit vector in the vertical (up) direction, and Q is the (nondimensional) spatially-varying internal heating function that has a mean (nondimensional) value of 1.0 (defined later). Note that due to the absence of a fixed temperature scale, T is nondimensionalized using a heating-derived scale:

$$T_{scale} = \frac{D^2 < Q >}{C_p \kappa} \tag{4}$$

The key parameter in this scaling study is Ra_Q, the Rayleigh number for internal heating, given by:

$$Ra_Q = \frac{\rho g \alpha < Q > D^5}{\eta \kappa^2 C_p} \tag{5}$$

where the meaning of the symbols and representative values are given in Table 1. These representative values can be used to calculate bounds on Ra_Q. The minimum possible Ra_Q of 6.75×10^{11} occurs for D=50 km and $\eta=10^{12}$ Pa s, while the maximum value of 1.1×10^{16} occurs for D=100 km and $\eta=10^9$ Pa s). A 'typical' value is thus $Ra_Q \sim 10^{14}$. It is worth emphasizing that these heating-based values of the Rayleigh number are much higher than the more conventional temperature-based values for equivalent convective vigor.

The key complexity in Io's asthenosphere is the non-uniform distribution of tidal heating Q, which is here decomposed into orthogonal azimuthal (x,y) and radial (z) components:

$$Q(x,y,z) = \Xi(x,y) \quad (z) \tag{6}$$

A sinusoid is chosen to mimic the horizontal tidal heating variation going from a maximum to a minimum. In two-dimensional calculations this is:

$$\Xi(x) = 1 + \cos\left(\frac{\pi x}{L_x}\right) \tag{7}$$

where L_x is the length of the box in the x-direction (the height is 1.0), while in three-dimensions it is:

$$\Xi(x,y) = \left[1 + \cos\left(\frac{\pi x}{L_x}\right)\right]\left[1 + \cos\left(\frac{\pi y}{L_y}\right)\right], \tag{8}$$

where L_y is the length of the domain the y-direction, which for the single 3-D case presented here, is equal to L_x. The focusing of dissipation near the upper and lower boundaries [*Segatz et al.*, 1988] is approximated by exponentials:

$$(z) = \frac{3}{1 - \exp(-6)}\left[\exp(-6z) + \exp(-6(1-z))\right] \tag{9}$$

In some cases heating is assumed to be uniform with z (i.e., $\Re$=1). Note that the volume-averaged heating rate given by equations (6)-(9) is equal to 1.0.

Time-dependent solutions are obtained using the finite-volume multigrid code STAG3D described elsewhere [*Tackley*, 1993; *Tackley*, 1996a], run on a Beowulf cluster of PCs at UCLA. Cases were run until a statistically steady-state was obtained, i.e., until diagnostics like mean temperature and rms. velocity stopped displaying a secular trend and the mean surface heat flow fluctuated around the volume-averaged internal heating rate of 1.0. This often required hundreds of thousands of time steps, particularly at high Rayleigh number and resolution. In order to speed the process up, cases were started at fairly course resolution then stepped up by a factor of 2 in resolution whenever they reached secular equilibrium. This was repeated until diagnostics did not change significantly at the next

resolution. The final resolution depended on Ra_Q, as listed in Table 2.

TABLE 2: Cases and numerical resolution

Ra_Q	Aspect Ratio	nx,nz
10^4	15	256,32
10^5	15	256,32
10^6	15	512,64
10^7	15	1024,64
10^8	15	2048,128
10^8	30	2048,64
10^8	60	4096,64
10^9	15	4096,256
10^{10}	15	4096,256

Results

Temperature fields

Figure 1a.-g. shows snapshots from a sequence of cases with Rayleigh number increasing from 10^4 to 10^{10}. At the lowest Ra_Q (Figure 1a.) the flow is steady-state and has a cellular structure. The highest temperature anomalies are at the left hand side of the domain where the highest internal heating rates occur while the right of the domain is cold. As Ra_Q is increased this cellular structure breaks down into a domain-wide mean flow with superimposed small-scale instabilities, a pattern that is established by $Ra=10^7$ (Figure 1d.). It is possible that with free-slip instead of rigid boundaries, the mean flow would get established at lower Ra_Q. The small-scale instabilities are most vigorous from the upper boundary layer although some do arise from the lower part of box despite the insulating lower boundary, because of the concentrated heating there. Their spacing decreases with Ra_Q, as studied by [*Tackley*, 1996b]. The descending instabilities are tilted towards the right by the mean flow. As Ra_Q is increased further, this mean flow distributes the heating across the domain, so that the temperature difference between the right- and left-hand sides of the domain decreases. The right side becomes relatively warm despite the absence of internal heating there.

Similar cases but with vertically-uniform heating are shown in Figure 1h.-n. They look similar to the previous cases but the middle of the asthenosphere is generally somewhat warmer. The similarity of these slices to Figure 1a.-g. indicates that the vertical non-uniformity in heating has only a small effect.

A curious feature of this mean-flow convection is that a temperature stratification develops, with hot, rightward-traveling material overlaying colder, leftward-traveling material. This is particularly visible at intermediate Ra_Q of around 10^7-10^9 (Figure 1e.-f.). Figure 2 shows horizontally-averaged temperature profiles for the cases with boundary-focused (Equation 9) heating. The raw temperature profiles (Figure 2a.) show mainly that temperatures decrease with increasing Ra_Q and fixed total heat input, which is well known from previous studies of internally-heated convection (e.g., [*Parmentier et al.*, 1994]). However, it is useful to quantify this for extrapolation to Io. Taking the maximum temperature in each iotherm and performing a least-squares fit to a power-law dependence on Ra_Q yields:

$$\langle T \rangle_{\max} = 1.9152 Ra_Q^{-0.2147} \quad (10)$$

where <> denotes horizontal averaging.

Most interesting is the degree of subadiabaticity or superadiabaticity, which is clearly visible in Figure 2b., in which temperature profiles have been normalized to have a maximum of 1.0. This shows that a superadiabatic internal temperature profile at low Ra_Q of 10^4, becomes increasingly subadiabatic between Ra_Q of 10^5 and 10^7, then decreasingly subadiabatic for Ra_Q above 10^8. The dotten line joining the temperature minima in Figure 2b brings out this trend more clearly. Regular internally-heated convection displays decreasing subadiabaticity with increasing Ra_Q throughout the range [*Parmentier et al.*, 1994]. Therefore the subrange $Ra_Q=10^5$-10^7 in the present calculations is unusual, which can be attributed to the development of a mean flow causing temperature stratification.

Heat flux

The surface heat flux distribution for the cases with boundary-focused heating are plotted in Figure 3a., while those for vertically-uniform heating are plotted in Figure 3b. The heat flux is averaged over 20-50 snapshots taken from the last part of each run. Note that the average heat flux is always 1.0.

The steady cellular pattern at low Ra_Q results in large (~ factor 2) spatial fluctuations in the surface heat flux near the left of the domain, and almost zero heat flux at the right of the domain. Increasing Ra_Q results in smaller (both in amplitude and scale) fluctuations in the surface heat flux and associated warming of the right side of the box, particularly for $Ra_Q > 10^6$). The heat flux becomes more uniform (more horizontal on the graph) with increasing Ra_Q. At $Ra_Q=10^{10}$ the heat flux varies from ~1.25 (left side) to ~0.75 (right side), whereas the heat input is always 2.0 (left side) to 0 (right side).

A goal of this paper is to develop a scaling for this smearing out of the surface heat flow by convection. Of most interest is the long-wavelength variation in heat flux. This is quantified using the average heat flux gradient, measured from the curves in Figure 3a.-b. by least-squares fitting of a straight line. The resulting heat flux gradients are plotted as a function of Ra_Q in Figure 4a.-b. Two regimes are visible from the plot: the constant heat-flux gradient regime at $Ra_Q<10^6$, and the decreasing heat flux gradient regime at $Ra_Q>10^6$. Physically, the transition between the two regimes corresponds to the breakdown of the cellular convection into a mean flow with small-scale instabilities.

The five points in the mean-flow regime are well fit by a power-law (i.e., a straight line in log-log space as Figure 4), and the resulting fit is plotted as a dashed line. The results are:

$$\frac{dF}{dx} = 2.869 \; Ra_Q^{-0.2105} \quad (11)$$

for boundary-focused heating and

$$\frac{dF}{dx} = 4.413 \; Ra_Q^{-0.2448} \quad (12)$$

for vertically-uniform heating. Note that these apply to long-wavelength variations, not variations associated with small-scale instabilities. The physical cause of these scalings is discussed later. In a previous study in 3-D spherical geometry and at lower Ra_Q [*Tackley et al.*, 2001], somewhat lower exponents averaging -0.189 were obtained. Those exponents were, however, for rms. or peak-to-peak heat flux variation, which are affected by small-scale features, unlike the long-wavelength variation considered here.

Width of domain

Given the uncertainties in the actual effective aspect ratio of Io's asthenosphere, it is important to determine whether these heat flux gradient scalings are valid for any domain width. This has been investigated by running two additional cases at $Ra_Q=10^8$ with aspect ratios twice and four times the standard aspect ratio (i.e., L_x=30 and 60 respectively). Temperature field snapshots (Figure 1o.-p.) show similar behavior to the L_x=15 case (Figure 1e.) but with an increasingly larger variation in temperature across the box. Surface heat flux is plotted in Figure 5 for the three different aspect ratios. For L_x=30 there is a nearly linear heat flux variation across the domain, with a gradient that is very similar to the gradient in the standard, L_x=15 case. For L_x=60 the heat flux flattens out at each end of the box (to ~2 and ~0 respectively, the value of the heating rate), but has a maximum gradient near the center of the box that is almost as large as the gradient in the smaller aspect ratio cases. Thus, it appears that the maximum heat flux gradient criterion applies to any domain width, unless the domain is wide enough that the maximum possible heat flux variation (i.e., $L_x\partial F/\partial x$) is larger than the variation of tidal heating (2 in these 2-D cases).

Three dimensions

Can the above scaling, derived from two-dimensional simulations, be applied to the real, three-dimensional situation in Io? To investigate this, the $Ra_Q=10^7$ case was run in 3-D geometry. The temperature field in plan view (Figure 6a.) shows a dramatic pattern of linear, flow-aligned small-scale instabilities radiating from the region of maximum heating to the region of minimum heating. The planform is consistent with that observed in a full 3-D spherical shell [*Tackley et al.*, 2001], giving confidence in the applicability of Cartesian geometry to investigate the basic dynamics. The small-scale instabilities prefer to be aligned with the flow direction, which is not possible in 2-D. In cross-section (Figure 6b.) the overall structure looks similar to the 2-D version (Figure 1d.) but the small-scale instabilities are less clearly visible because they prefer to be aligned with the flow direction.

The surface heat flux distribution, plotted in Figure 7a., resembles the near-surface temperature distribution plotted in Figure 6a. When averaged in the *y*-direction, this closely overlies the heat flux profile obtained in the 2-D case (Figure 7b.), giving confidence in the use of 2-D scalings in 3-D geometry. However, when the heat flux along the region near y=0 is plotted (i.e., from (x,y)=(0,0) to (15,0), averaged over 10 cells in y), the heat flux is substantially higher, and has a steeper gradient, than in the 2-D case. This is not surprising because the scalings were obtained for a situation in which the mean heating rate is 1.0, whereas for this profile the mean heating rate is 2.0 (equation 8). Thus, it might be expected that the heat flux along this profile should be twice as high, multiplied by a correction of factor $2^{-0.2105}$ to account for the doubling in profile Rayleigh number, a net expected increase of factor 1.73. This appears to be consistent with curve in Figure 7b. In conclusion, the two-dimensional scalings appear to work for 3-D cases provided adjustments are made for the average heating in the chosen profile.

Velocities

Profiles of horizontal averages of the x-velocity and |z-velocity| are plotted for $Ra_Q=10^4$, 10^6 and 10^{10} in Figure 8a.-c. For the cellular convection at $Ra_Q=10^4$ (Figure 8a.), vertical velocities are larger than horizontal velocities, but by $Ra_Q=10^6$ (Figure 8b.) the development of a mean flow has generated horizontal velocities that are substantially larger than the vertical velocities. This difference in horizontal and vertical velocities increases as Ra_Q is further increased, until by $Ra_Q=10^{10}$ (Figure 8c.), horizontal motion is many times faster than vertical motion. A scaling is obtained by taking the maximum horizontally-averaged velocity for each Ra_Q (plotted in Figure 8d.) and obtaining a (power-law) least-squares fit to its variation with Ra_Q in the range 10^7 to 10^{10} is obtained (plotted as dashed lines). These fits are:

$$< v_x >_{\max} = 0.1413 Ra_Q^{0.4857} \quad (13)$$

$$<| v_z |>_{\max} = 0.0971 Ra_Q^{0.4301} \quad (14)$$

where <> here denotes horizontal averaging.

Discussion

Comparison with previous theory

It is useful to review how vertical heat transport efficiency, as measured by the Nusselt number *Nu*, scales with Ra_Q. For simple internally-heated convection with an isothermal upper boundary driven by uniform internal heating, simple boundary layer theory (e.g., [*Turcotte and Schubert*, 1982]) gives a theoretical scaling of:

$$Nu \quad Ra_Q^{1/4} \quad (15)$$

The exponent of 0.2448 obtained in this study for horizontal transportation of heat by the mean flow for vertically-uniform heating is remarkably close to this exponent of 1/4, implying that vertical and horizontal transport of heat scale proportionally. In the cases with boundary-focused heating the exponent is slightly lower at 0.2105, but it is not uncommon for actual exponents to be lower than the idealized scalings.

In the simulations presented here, heating rate is kept fixed (with a mean of 1.0) while Ra_Q is varied, so changes in Ra_Q may physically correspond to (inverse) changes in viscosity. F in the above scalings should thus be thought of as normalized heat flux, and to apply to situations where the

mean heat flux is not 1.0, the mean heat flux should be incorporated as follows:

$$\frac{1}{\langle F \rangle}\frac{dF}{dx} = 4.413 Ra_Q^{-0.2448} \quad (16)$$

Applying to another commonly-modeled scenario: If changes in Ra_Q were accommodated in such a manner as to keep the mean internal temperature roughly constant, then $<Q>$ and hence $<F>$ would increase roughly as $Ra_Q^{1/4}$ and dF/dx would be constant with Ra_Q.

The power-law exponent of -0.2147 for temperature (Equation 10) is very similar in magnitude to the exponent of 0.2105 for heat flux gradient, again implying the similarity of horizontal and vertical heat transfer scalings (since internal temperature is expected to scale as the inverse of Nusselt number).

The theoretical scaling for velocities (e.g., [*Turcotte and Schubert*, 1982]) is:

$$v \quad Ra_Q^{1/2} \quad (17)$$

The experimental exponent for horizontal velocity (0.4857) is close to this, but for vertical velocity the exponent is somewhat lower (0.4301).

Analytical derivation of mean flow scalings

The above scalings for mean flow convection can be straightforwardly derived by assuming that packets of material become hot at the left side of the box then move across the upper half of the domain with uniform horizontal velocity u, losing heat as they do so by small-scale convection obeying the standard internally-heated convection scalings given above. If it is further assumed that the temperature difference across the domain is small, as is the case at asymptotically high Rayleigh number, then rate of temperature decrease and hence heat loss (flux) can be assumed to be constant across the domain, with heat flux F=1. A reasonable starting point is to assume that local heat flux is related to the local interior temperature T_u such that:

$$\frac{1}{F}\frac{\partial F}{\partial x} = \frac{\partial F}{\partial x} = \frac{1}{T_u}\frac{\partial T_u}{\partial x} \quad (18)$$

where the internally-heated convection theory referenced above predicts that T_u decreases with increasing Ra_Q as:

$$T_u \quad Ra_Q^{-1/4} \quad (19)$$

and the horizontal temperature gradient is related to the heat flux and velocity by:

$$\frac{\partial T_u}{\partial x} \quad \frac{F}{u} \approx \frac{1}{u} \quad (20)$$

Combining these, one obtains:

$$\frac{\partial F}{\partial x} \quad \frac{Ra_Q^{1/4}}{u}. \quad (21)$$

To determine u, it is reasonable to assume that the total force required to drive the viscous flow (proportional to u, the length of the domain L_x and the viscosity), is equal to the long-wavelength gravitational force available to drive the flow (proportional to the horizontal temperature difference across the box $L_x \partial T / \partial x$), hence:

$$\frac{uL_x}{Ra_Q} \quad L_x \frac{\partial T_u}{\partial x} \quad (22)$$

which, using (20), leads to:

$$u \quad Ra_Q^{1/2} \quad (23)$$

and a heat flux gradient (from (21)) of

$$\frac{\partial F}{\partial x} \quad Ra_Q^{-1/4} \quad (24)$$

Equations (23) and (24) are consistent with the scalings obtained in the numerical experiments presented in this paper.

Scaling to Io

For a two-phase system such as Io's asthenosphere, it may be more appropriate to use "effective" values of thermodynamic parameters such as thermal expansivity and heat capacity rather than the values given in Table 1. These "effective" or "apparent" values take into account the changes in solid fraction that accompany changes in temperature. [*Solomatov and Stevenson*, 1993a] derived these for peridotite with a pyroxene solid solution in the context of an early terrestrial magma ocean, finding that, depending on temperature and ratio of components, the effective thermal expansivity and heat capacity exceed phase-fraction averaged versions by factors of 10-60 and 2.5-15 respectively. Taking "typical" values of 12 and 3 times the Table 1 values leads to a reduction in temperature scale (Equation (4)) by a factor of 3 and an increase in Rayleigh number (Equation (5)) by a factor of 4. The scalings below start by using Table 1 values then give the values for effective thermodynamics parameters.

Heat flux variations. Using equation (11), the expected heat flux variations for Io's asthenosphere can be estimated. For the "typical" Ra_Q of 10^{14}, the normalized heat flux gradient is 3.2×10^{-3}, which, for an aspect ratio of between 15 and 30, gives 4.9 to 9.7% variation in heat flux. The minimum Ra_Q (6.75×10^{11}) gives 27% variation over an aspect ratio of 30, while the maximum Ra_Q (1.1×10^{16}) gives 1.8%

variation over an aspect ratio of 15. Using the slightly higher Ra_Q that results from "effective" (two-phase) thermodynamic coefficients reduces these estimates by 25%.

Temperature fluctuations. Although the obtained equation for temperature (Equation 10) refers to maximum horizontally-averaged temperature (relative to the temperature at the upper boundary), it gives a rough bound on the size of temperature fluctuations associated with convection. For dimensionalization, the temperature scale (Equation 4) is 30583, 45875, or 61167 K for asthenosphere thicknesses of 50, 75, or 100 km respectively and the Table 1 heat capacity. At $Ra_Q=10^{14}$, the nondimensional $T_{max}=1.9\text{x}10^{-3}$, corresponding to a dimensional temperature of 86 K. For the extreme Ra_Q, T_{max} ranges from 169 K to 42 K. For the effective (two-phase) expansivity and heat capacity these estimates are reduced by 75% to between 41 K and 10 K with a "typical" value of 21 K.

Velocities. Nondimensional velocities are scaled to κ/D, which is, for example, 10^{-11} m/s for a 100 km thick asthenosphere. Using Equation (13) with $Ra_Q=10^{14}$, a maximum mean horizontal velocity of $8.9\text{x}10^5$ is obtained, corresponding to 281 m/year. Extreme values of Ra_Q give a range of 25 m/year to 2800 m/year. Using effective properties these estimates are increased by a factor of ~2, giving 50 to 560 to 5600 m/year. These velocities give an upper bound on the speed at which surface volcanism might move, if surface volcanoes are related to individual convective features. An interesting question is: How much might the system have changed between Voyager observations and Galileo observations, an approximately 20 year time interval? The above velocities would give motion of between 1 km and 112 km over this time period, which may be rather small to detect observationally.

Conclusions and Future Directions

High Rayleigh number convection driven by horizontally-varying volumetric heating is characterized by a mean flow with superimposed small-scale instabilities. The effect of the mean flow is to progressively even out the surface heat flux as Rayleigh number is increased. Quantities such as long-wavelength horizontal heat flux gradient, interior temperature, and vertical and horizontal velocities have powerlaw scalings with Ra_Q, at least in the Ra_Q range 10^7 - 10^{10}, and this can be used to extrapolate to expected conditions in Io's asthenosphere. Such an extrapolation leads to predicted surface heat flux variations of several percent, temperature variations of order 10s of K, and mean flow velocities of 50-5600 m/yr.

This small variation in surface heat flux may (as discussed in [*Tackley et al.*, 2001]) be consistent with the observed subtle distributions of volcanoes and mountains, which to first order occur everywhere [*Lopes-Gautier et al.*, 1999], but display clear patterns after being converted to a continuous distribution using a sliding window [*Schenk and Hargitai*, 1998; *Schenk et al.*, 2000; *Tackley et al.*, 2001]. The volcano distribution resembles the asthenosphere heating function, supporting asthenospheric heating as the dominant tidal dissipation mode [*Ross et al.*, 1990], whereas the mountain distribution is similar but phase shifted by 90° in longitude, consistent with mountains preferentially occurring in regions of crustal compression and convergence associated with convective downwellings. The fairly small temperature variations indicate that the peak temperature of silicate volcanism is not expected to vary substantially from place to place, whereas the estimated flow velocities suggest that any changes due to asthenospheric advection may be too small to detect over the Voyager to Galileo timescale.

There are some possible problems with applying this analysis directly to Io. Firstly, the validity of treating a melt-solid mush as a single entity with a single effective viscosity is not certain- ideally the segregation of melt and solid should be resolved (e.g., [*McKenzie*, 1984; *Sparks and Parmentier*, 1991; *Spiegelman*, 1993]), a computationally demanding task. However, analyses of magma ocean dynamics [*Solomatov and Stevenson*, 1993a; *Solomatov and Stevenson*, 1993b] indicate that this approximation is reasonable if the crystals are separated because the convective velocities are much higher than crystal settling velocity, and viscous dissipation due to crystal settling should be negligible for a small body like Io. Secondly, Io may not have an asthenosphere with well-defined upper and lower "rigid" boundaries, but rather have a gradual increase in viscosity (due to decreasing melt fraction) with depth, a model recently favored by [*Keszthelyi et al.*, 1999]. Thirdly, it is possible that transitions in the convective regime occur at higher Rayleigh number than has been attained here, which may alter the scaling relationships. Such changes have been documented for basal-heated convection by [*Hansen et al.*, 1990] and [*Vincent and Yuen*, 2000].

Thus, the present, idealized calculations should perhaps be viewed as a preliminary estimate of convective processes in Io's asthenosphere, and endeavors made to determine the effects of melt:solid segregation, other plausible internal structure models, and increased convective vigor.

Acknowledgments. Supported by the David and Lucile Packard Foundation. The author thanks Gerald Schubert and Gary Glatzmaier for starting him on Io research and Slava Solomatov and Louis Moresi for constructive reviews.

References

Carr, M.H., A.S. McEwen, K.A. Howard, F.C. Chuang, P. Thomas, P. Schuster, J. Oberst, G. Neukum, and G. Schubert, Mountains and calderas on Io: possible implications for lithosphere structure and magma generation, *Icarus*, *135* (1), 146-65, 1998.

Cassen, P.M., S.J. Peale, and R.T. Reynolds, Structure and thermal evolution of the Galilean satellites, in *Satellites of Jupiter*, edited by D. Morrison, pp. 93-128, The University of Arizona Press, Tucson, 1982.

Hansen, U., D.A. Yuen, and S.E. Kroening, Transition to Hard Turbulence In Thermal-Convection At Infinite Prandtl Number, *Phys. Fluids A*, *2* (12), 2157-2163, 1990.

Keszthelyi, L., A.S. McEwen, and G.J. Taylor, Revisiting the hypothesis of a mushy global magma ocean in Io, *Icarus*, *141* (2), 415-19, 1999.

Lopes-Gautier, R., A.S. McEwen, W.B. Smythe, P.E. Geissler, L. Kamp, A.G. Davies, J.R. Spencer, L. Keszthelyi, R. Carlson, F.E. Leader, R. Mehlman, and L. Soderblom, Active volcanism on Io: global distribution and variations in activity, *Icarus*, *140* (2), 243-64, 1999.

McEwen, A.S., L. Keszthelyi, P. Geissler, D.P. Simonelli, M.H. Carr, T.V. Johnson, K.P. Klaasen, H.H. Breneman, T.J. Jones, J.M. Kaufman, K.P. Magee, D.A. Senske, M.J.S. Belton, and G. Schubert, Active volcanism on Io as seen by Galileo SSI, *Icarus*, *135* (1), 181-219, 1998a.

McEwen, A.S., L. Keszthelyi, J.R. Spencer, G. Schubert, D.L. Matson, R. Lopesgautier, K.P. Klassen, T.V. Johnson, J.W. Head, P. Geissler, S. Fagents, A.G. Davies, M.H. Carr, H.H. Breneman, and M.J.S. Belton, High-temperature silicate volcanism on Jupiter's moon Io, *Science*, *281* (5373), 87-90, 1998b.

McKenzie, D., The Generation and Compaction Of Partially Molten Rock, *J. Petrol.*, *25* (3), 713-765, 1984.

Moresi, L.N., and V.S. Solomatov, Numerical investigation of 2d convection with extremely large viscosity variations, *Phys. Fluids*, *7* (9), 2154-2162, 1995.

Parmentier, E.M., C. Sotin, and B.J. Travis, Turbulent 3-D thermal convection in an infinite Prandtl number, volumetrically heated fluid - Implications for mantle dynamics, *Geophys. J. Int.*, *116* (2), 241-251, 1994.

Peale, S.J., P. Cassen, and R.T. Reynolds, Melting of Io by tidal dissipation, *Science*, *203* (4383). 892-894, 1979.

Ross, M., and G. Schubert, Tidal dissipation in a viscoelastic planet, *J. Geophys. Res.*, *91* (B4), 447-52, 1986.

Ross, M.N., and G. Schubert, Tidally forced viscous heating in a partially molten Io, *Icarus*, *64* (3), 391-400, 1985.

Ross, M.N., G. Schubert, T. Spohn, and R.W. Gaskell, Internal structure of Io and the global distribution of its topography, *Icarus*, *85* (2), 309-25, 1990.

Schenk, P., and H. Hargitai, Morphology and distribution of mountains on Io, *Bull. Amer. Astron. Soc.*, *30*, 1121, 1998.

Schenk, P., H. Hargitai, R. Wilson, A. McEwen, and P. Thomas, The mountains of Io: Global and geological perspectives from Voyager and Galileo, *J. Geophys. Res.*, *submitted*, 2000.

Schubert, G., T. Spohn, and R.T. Reynolds, Thermal histories, compositions and internal structures of the moons of the solar system, in *Satellites*, edited by J.A. Burns, and M.S. Matthews, pp. 224-292, The University of Arizona Press, Tucson, 1986.

Schubert, G., D.J. Stevenson, and K. Ellsworth, Internal structures of the Galilean satellites, *Icarus*, *47* (1). 46-59, 1981.

Segatz, M., T. Spohn, M.N. Ross, and G. Schubert, Tidal dissipation, surface heat flow, and figure of viscoelastic models of Io, *Icarus*, *75* (2), 187-206, 1988.

Solomatov, V.S., Scaling of temperature-dependent and stress-dependent viscosity convection, *Phys. Fluids*, *7* (2), 266-274, 1995.

Solomatov, V.S., and D.J. Stevenson, Nonfractional Crystallization Of a Terrestrial Magma Ocean, *Journal Of Geophysical Research-Planets*, *98* (E3), 5391-5406, 1993a.

Solomatov, V.S., and D.J. Stevenson, Suspension In Convective Layers and Style Of Differentiation Of a Terrestrial Magma Ocean, *Journal Of Geophysical Research-Planets*, *98* (E3), 5375-5390, 1993b.

Sparks, D.W., and E.M. Parmentier, Melt Extraction From the Mantle Beneath Spreading Centers, *Earth and Planetary Science Letters*, *105* (4), 368-377, 1991.

Spiegelman, M., Flow In Deformable Porous-Media .1. Simple Analysis, *Journal Of Fluid Mechanics*, *247*, 17-38, 1993.

Tackley, P.J., Effects of strongly temperature-dependent viscosity on time-dependent, 3-dimensional models of mantle convection, *Geophys. Res. Lett.*, *20* (20), 2187-2190, 1993.

Tackley, P.J., Effects of strongly variable viscosity on three-dimensional compressible convection in planetary mantles, *J. Geophys. Res.*, *101*, 3311-3332, 1996a.

Tackley, P.J., On the ability of phase transitions and viscosity layering to induce long-wavelength heterogeneity in the mantle, *Geophys. Res. Lett.*, *23*, 1985-1988, 1996b.

Tackley, P.J., G. Schubert, G.A. Glatzmaier, P. Schenk, J.T. Ratcliff, and J.-P. Matas, Three-dimensional simulations of mantle convection in Io, *Icarus*, *149* (1), 79-93, 2001.

Travis, B., S. Weinstein, and P. Olson, 3-dimensional convection planforms with internal heat generation, *Geophys. Res. Lett.*, *17* (3), 243-246, 1990.

Turcotte, D.L., and G. Schubert, *Geodynamics: Applications of Continuum Physics to Geological Problems*, Wiley, New York, 1982.

Vincent, A.P., and D.A. Yuen, Transition to turbulent thermal convection beyond Ra=10^10 detected in numerical simulations, *Physical Rev. E*, *61* (5), 5241-6, 2000.

Yoder, C.F., How tidal heating in Io drives the Galilean orbital resonance locks, *Nature*, *279* (5716), 767-70, 1979.

Yoder, C.F., and S.J. Peale, The tides of Io, *Icarus*, *47* (1), 1-35, 1981.

Figure Captions

Figure 1. Snapshots of the temperature field for various cases. The color bar is normalized to the maximum temperature in each snapshot. The left column shows cases with boundary-focused tidal heating and Ra_Q of (a) 10^4, (b) 10^5, (c) 10^6, (d) 10^7, (e) 10^8, (f) 10^9, (g) 10^{10}. The right column shows cases with vertically-uniform tidal heating and Ra_Q of (h) 10^4, (i) 10^5, (j) 10^6, (k) 10^7, (l) 10^8, (m) 10^9, (n) 10^{10}. The bottom plots that straddle both columns show cases with boundary-focused dissipation, $Ra_Q=10^8$ and aspect ratios of (o) 30 and (p) 60.

Figure 2. Horizontally-averaged temperature profiles ("Iotherms") for cases with boundary-focused heating and Rayleigh numbers ranging from 10^4 to 10^{10} (see legend). (a) The raw Iotherms, and (b) with each Iotherm normalized to its maximum value. The dotted line joins together temperature minima in the lower half of the domain.

Figure 3. Surface heat flux as a function of horizontal position x for all cases with aspect ratio 15. (a) Boundary-focused dissipation, (b) vertically-uniform dissipation.

Figure 4. Dependence of dF/dx on Ra_Q for (a) boundary-focused heating and (b) vertically-uniform heating. The dashed lines are least-squares fits to the points for $Ra_Q \geq 10^6$.

Figure 5. Surface heat flux vs. horizontal position x for cases with $Ra_Q=10^8$ and aspect ratios (L_x) of 15, 30, and 60.

Figure 6. Temperature field for the 3-D case with $Ra_Q=10^7$, from two different viewpoints.

Figure 7. Surface heat flux distributions for the 3-D case with $Ra_Q=10^7$. (a) Plotted as a function of horizontal position (x and y). (b) Plotted vs. x: y-averaged (solid line), along the line y=0 (dashed line), equivalent 2-D case for reference (dotted line).

Figure 8. Vertical profiles of horizontally-averaged v_x, and horizontally-averaged $|v_z|$, for (a) $Ra_Q=10^4$, (b) $Ra_Q=10^6$, (c) $Ra_Q=10^{10}$. (d) Maximum velocities in each profile plotted vs. Ra_Q, with least-squares fits to the higher-Ra_Q points. See text for details.

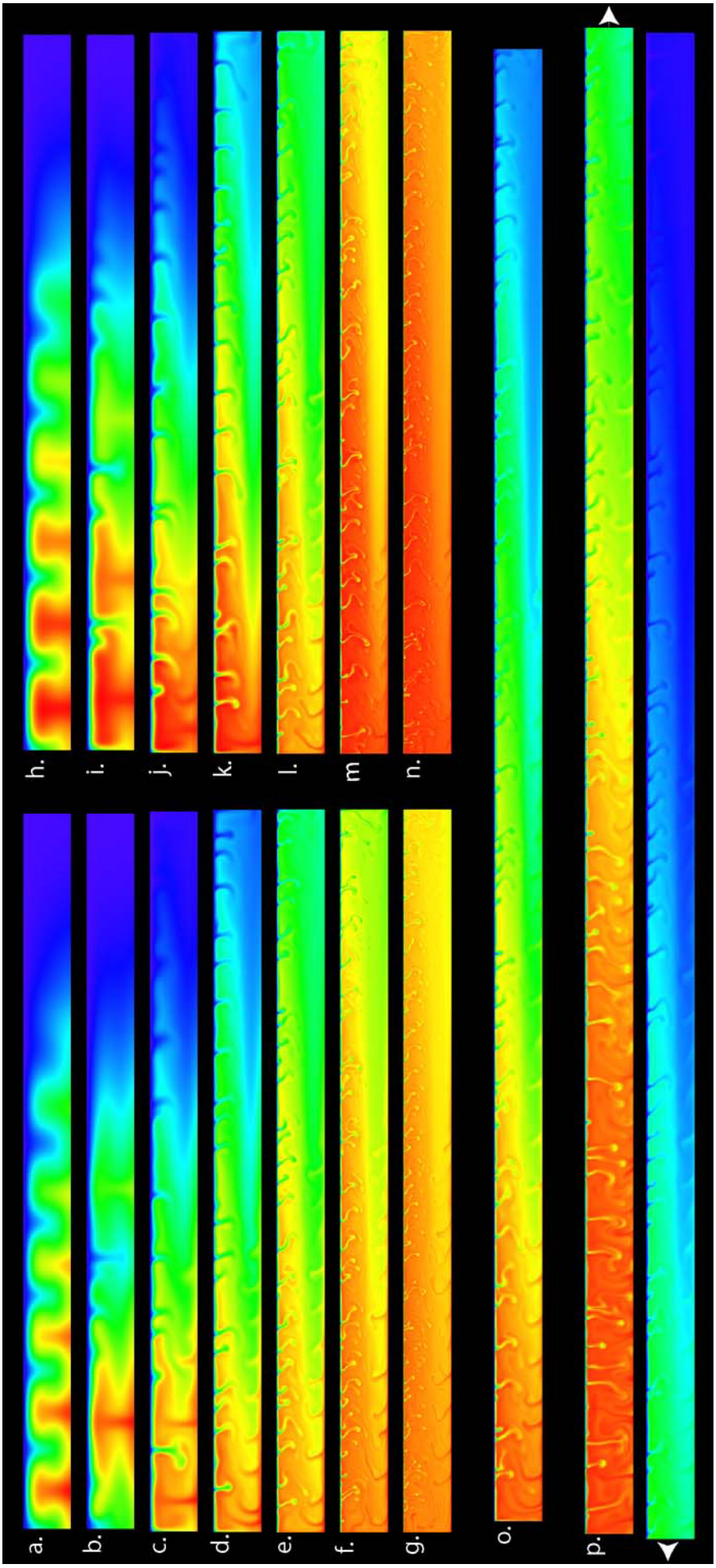

Figure 1

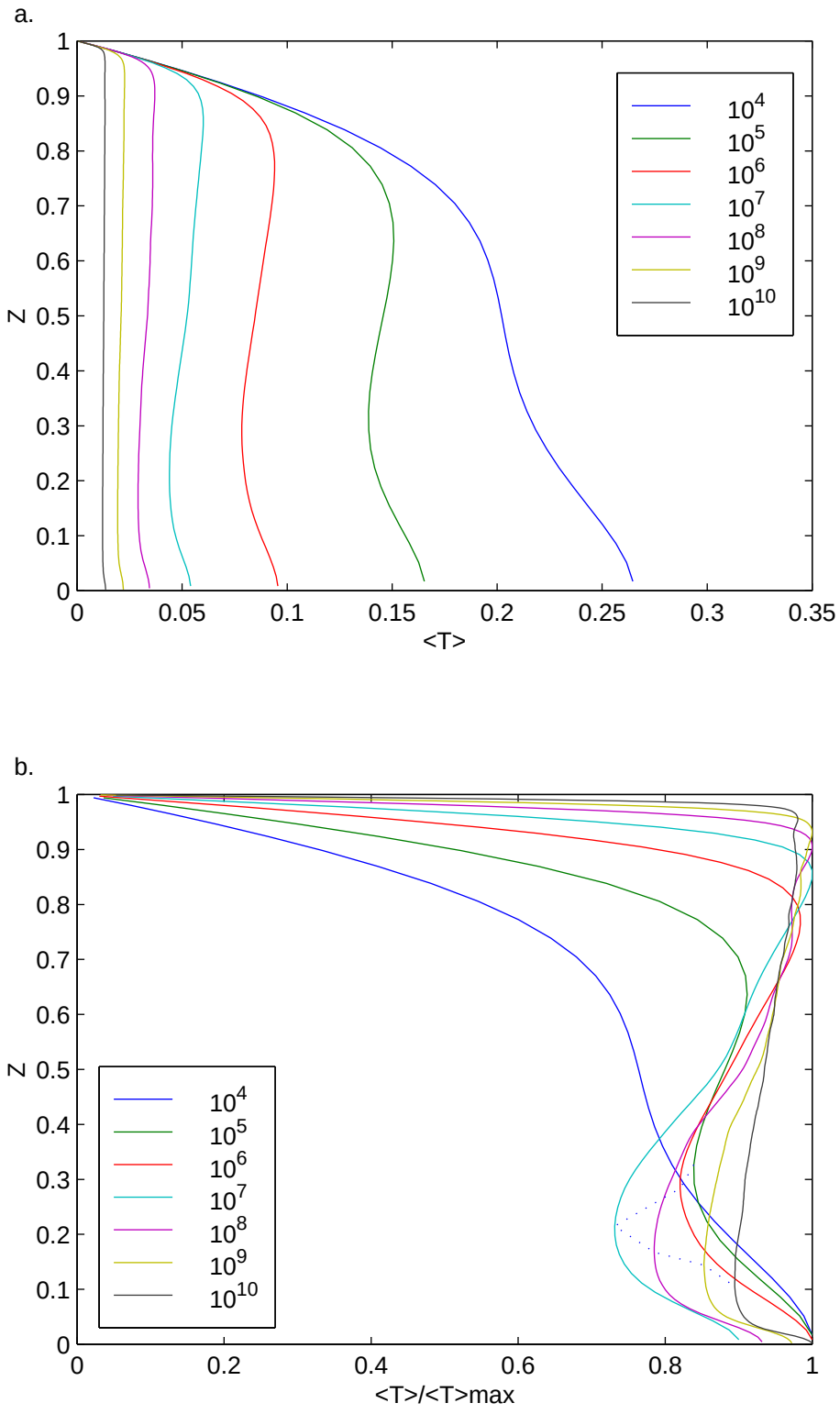
a.
Z
<T>
0
0.05
0.1
0.15
0.2
0.25
0.3
0.35
0.1
0.2
0.3
0.4
0.5
0.6
0.7
0.8
0.9
1
10^4
10^5
10^6
10^7
10^8
10^9
10^{10}
b.
Z
<T>/<T>max
0
0.2
0.4
0.6
0.8
1

Figure 2

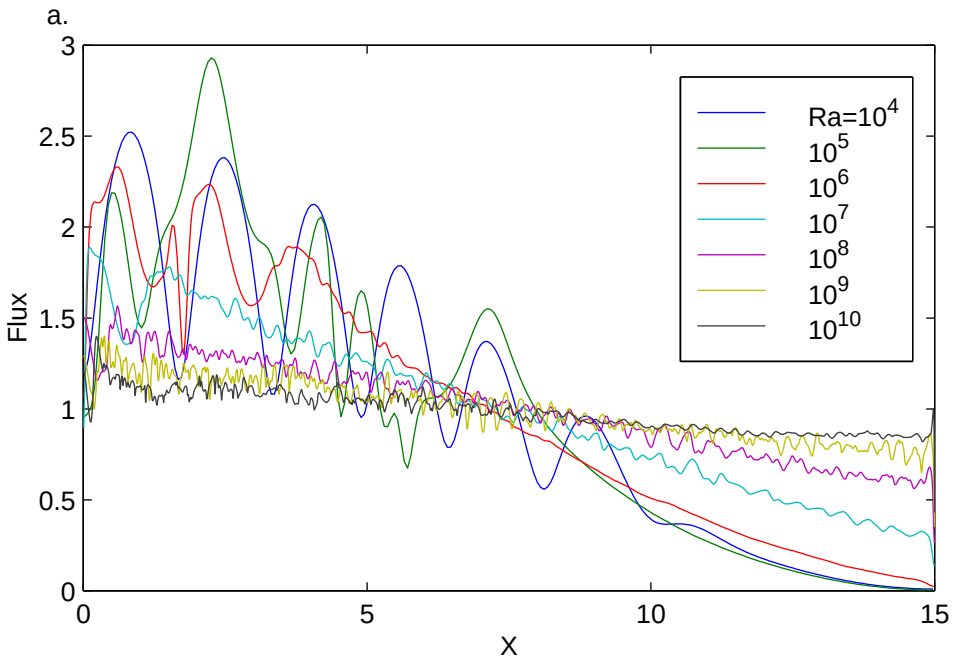
a.
Flux
X
0
0.5
1
1.5
2
2.5
3
0
5
10
15
Ra=10^4
10^5
10^6
10^7
10^8
10^9
10^10

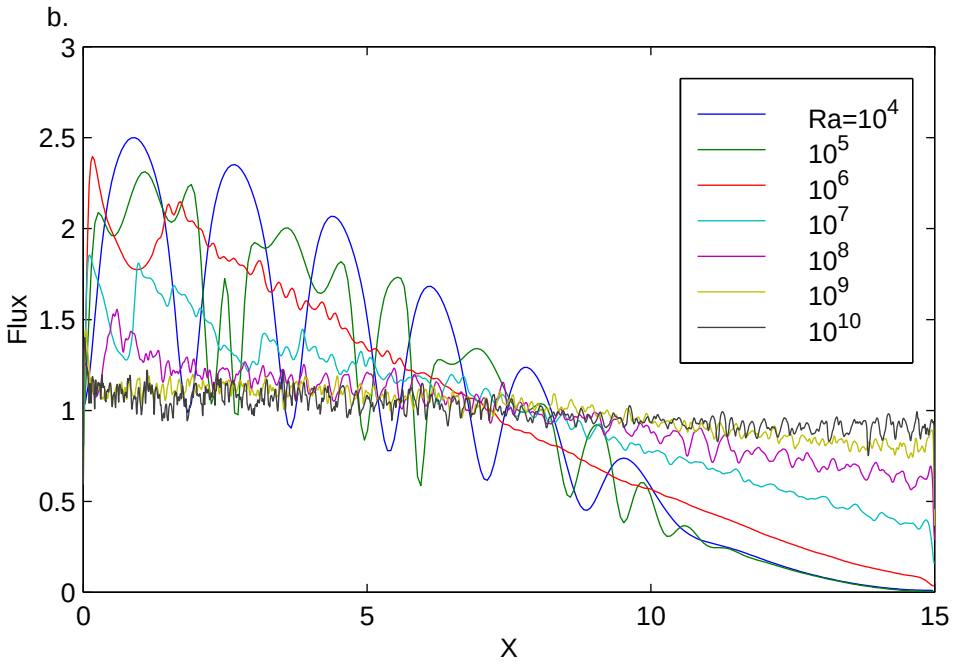
b.
Flux
X
0
0.5
1
1.5
2
2.5
3
0
5
10
15
Ra=10^4
10^5
10^6
10^7
10^8
10^9
10^10

Figure 3

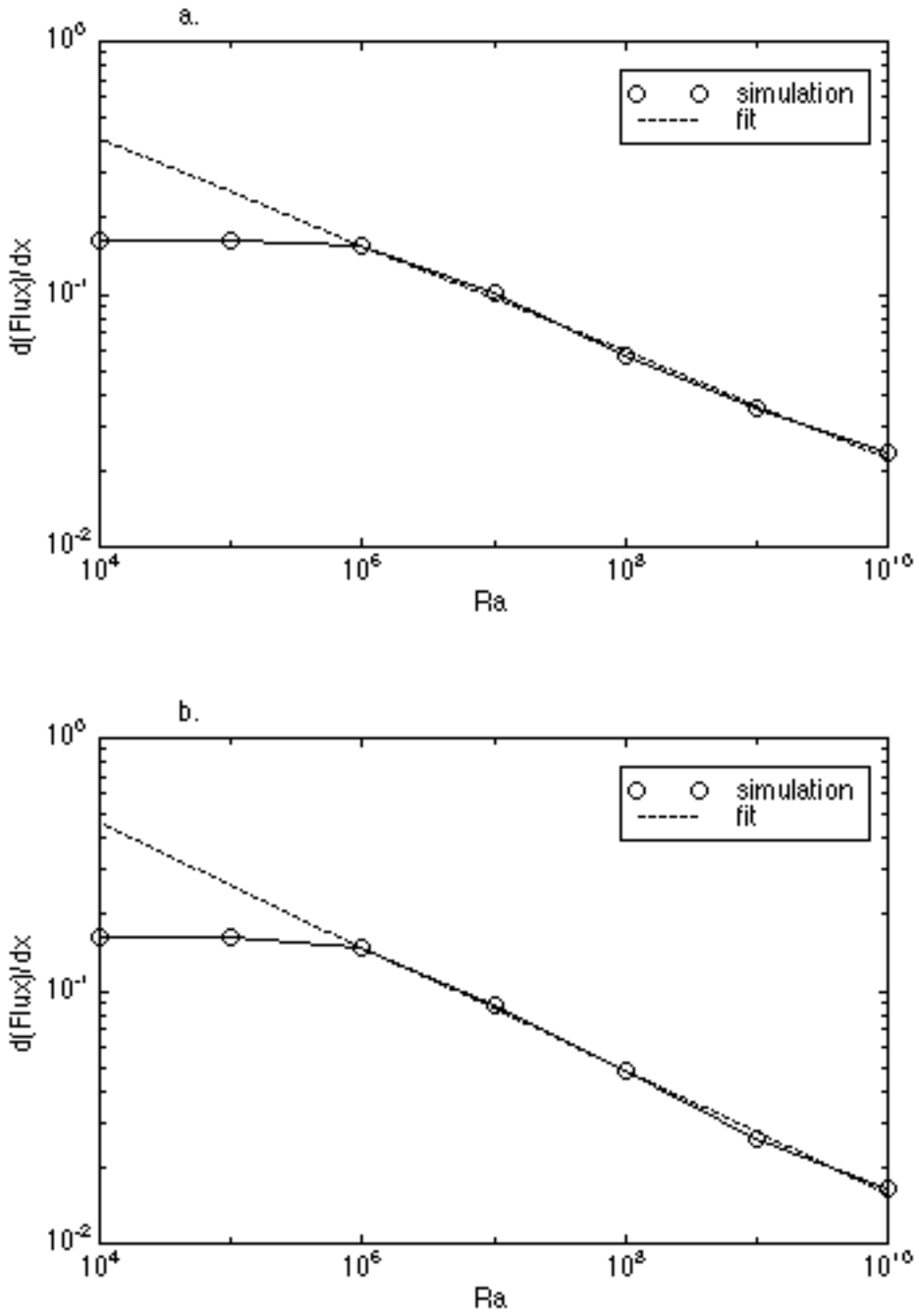

Figure 4

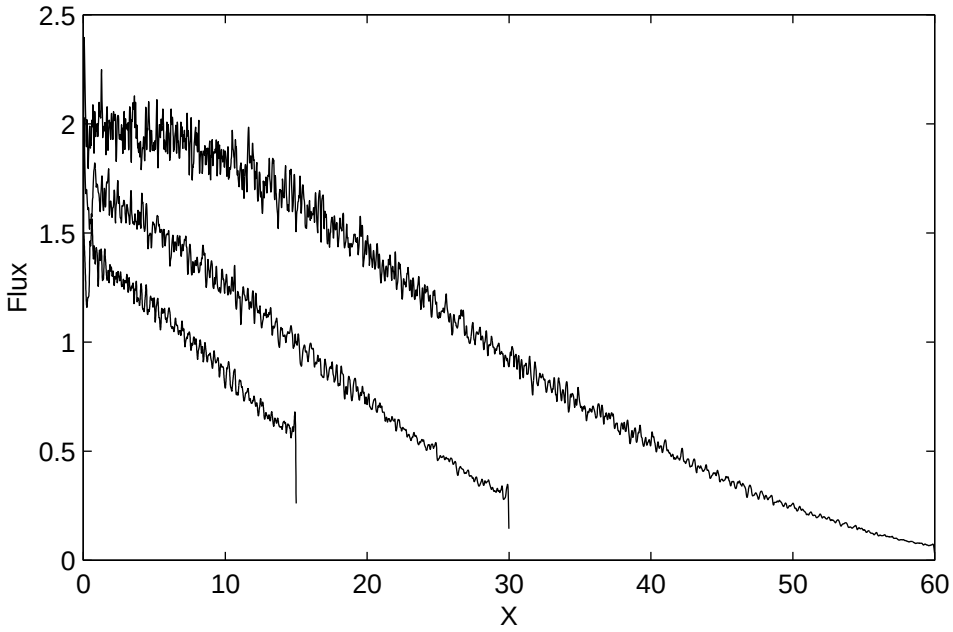

Figure 5

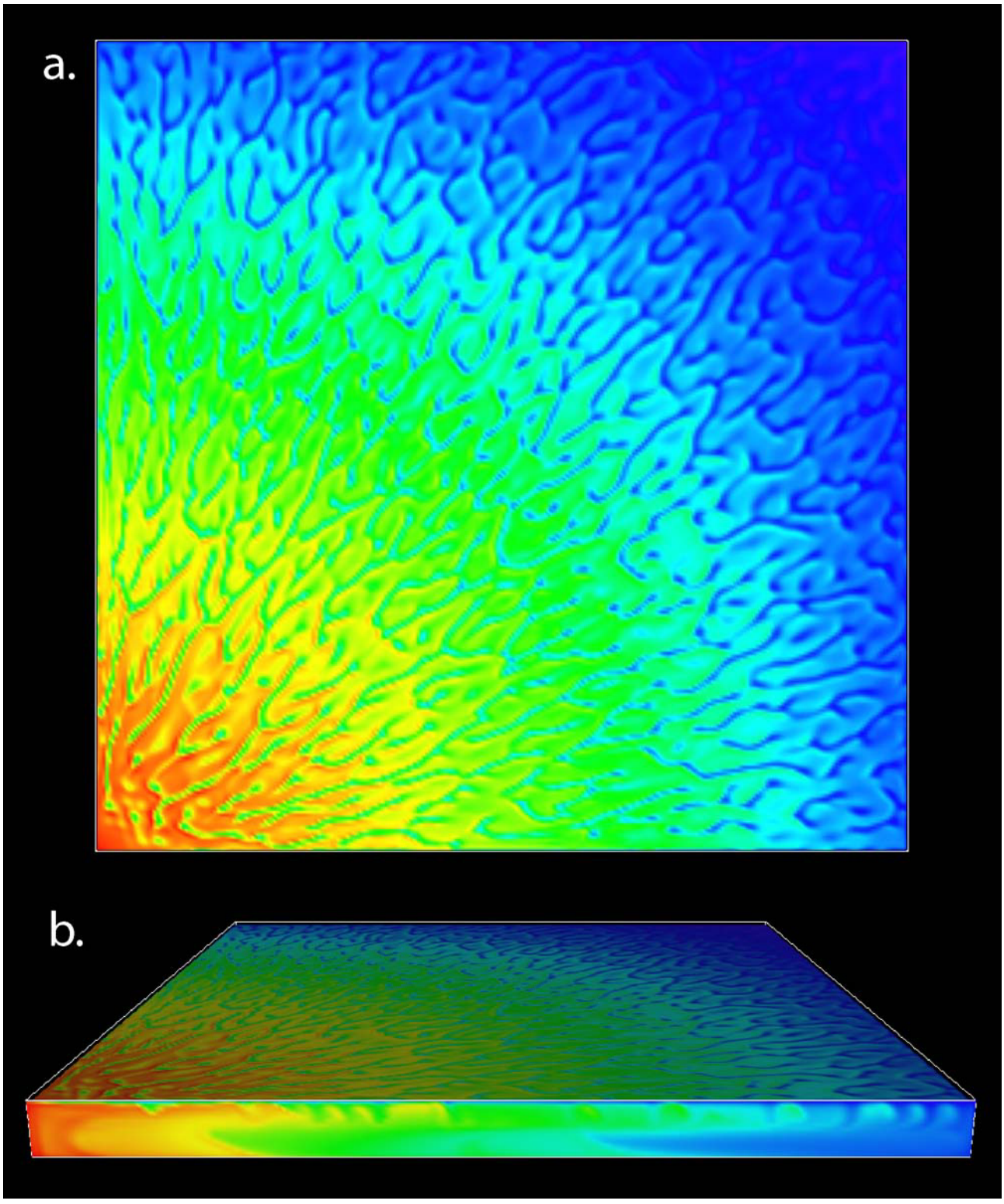

Figure 6

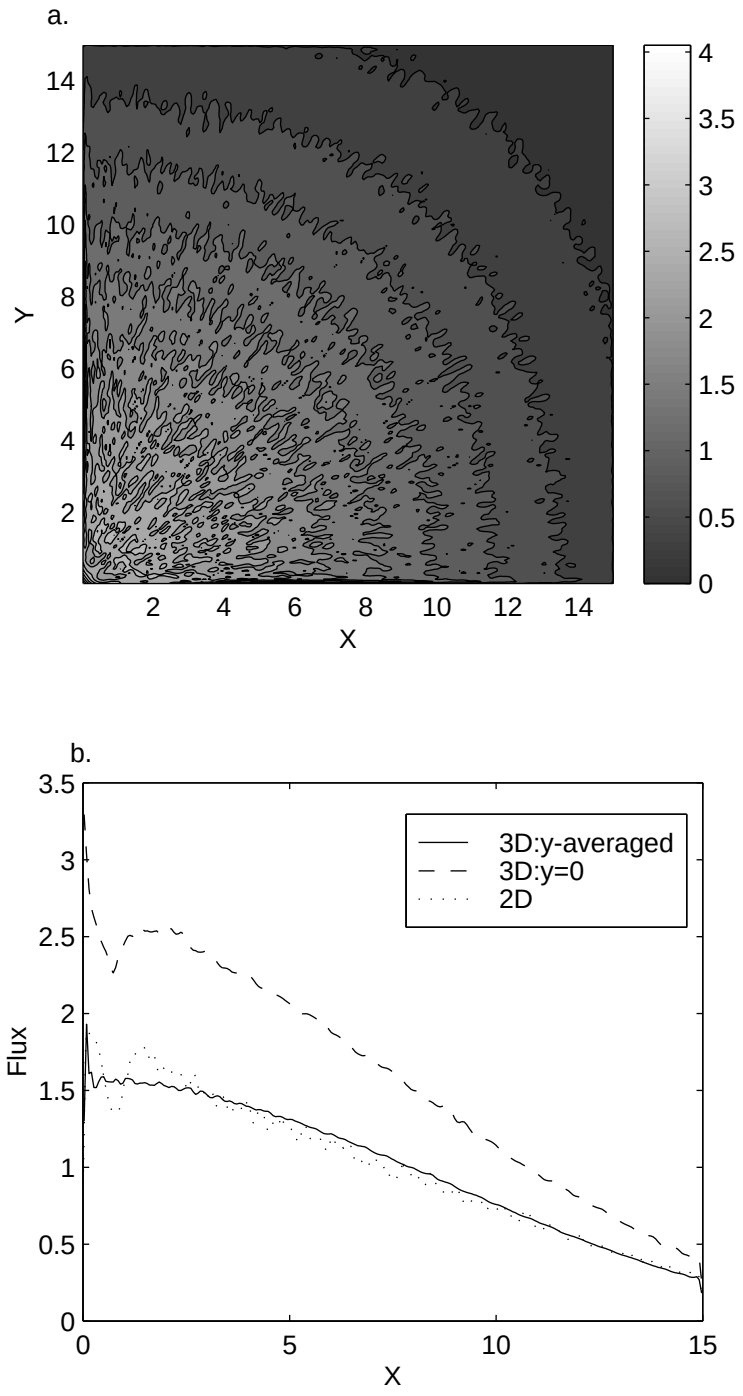
a.
Y
X
2
4
6
8
10
12
14
0
0.5
1
1.5
2
2.5
3
3.5
4
b.
Flux
X
3D:y-averaged
3D:y=0
2D
0
5
10
15
0.5
1
1.5
2
2.5
3
3.5

Figure 7

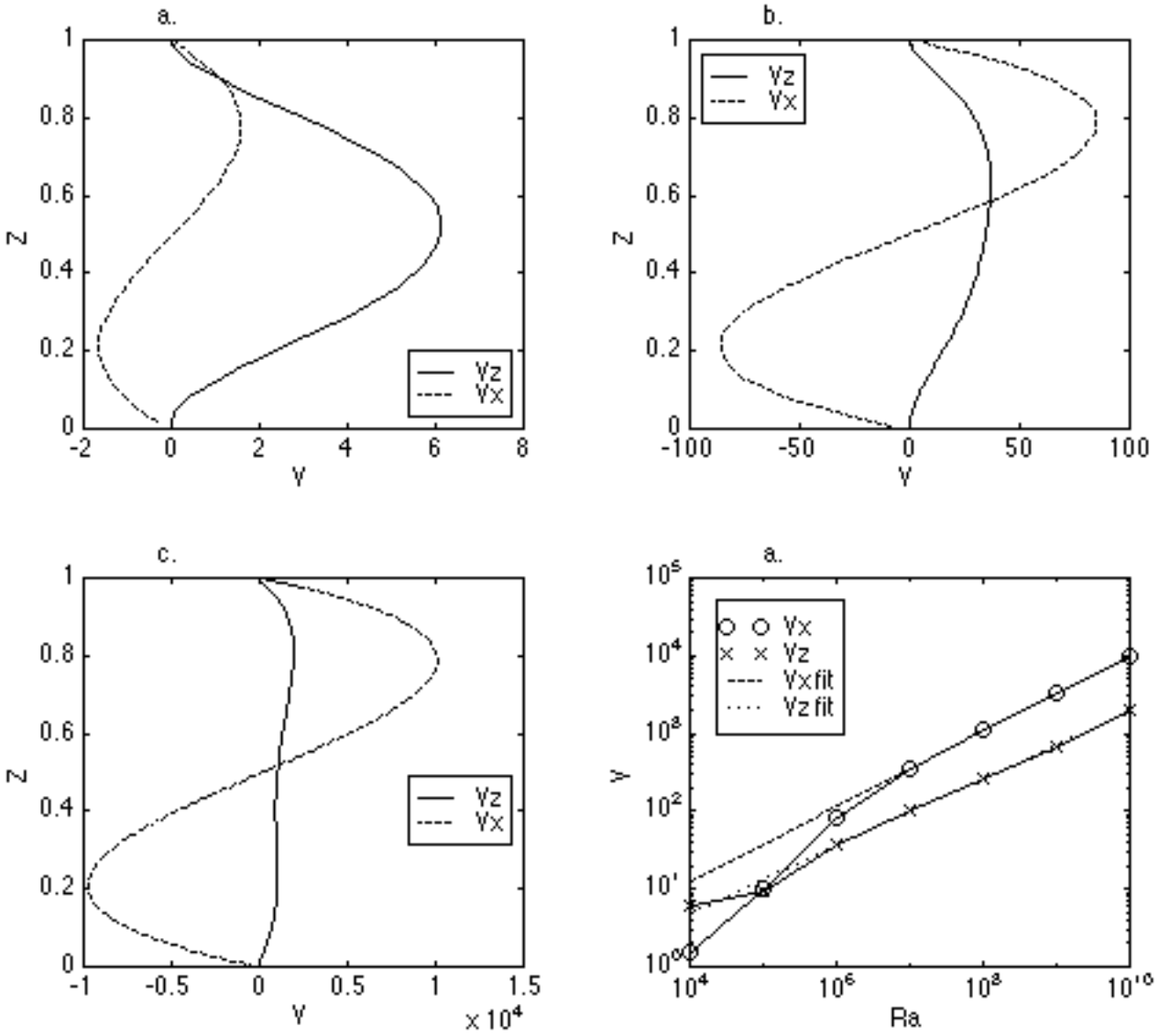

Figure 8